

Chirality manipulation of ultrafast phase switchings in a correlated CDW-Weyl semimetal

Bing Cheng,¹ Di Cheng,¹ Tao Jiang,¹ Wei Xia,^{2,3} Boqun Song,^{1,4} Martin Mootz,^{1,4} Liang Luo,¹ Ilias E. Perakis,⁵ Yongxin Yao,¹ Yanfeng Guo,^{2,3} and Jigang Wang^{1,4}

¹Ames National Laboratory, Ames, IA 50011 USA

²School of Physical Science and Technology, ShanghaiTech University, Shanghai 201210, China

³ShanghaiTech Laboratory for Topological Physics, Shanghai 201210, China

⁴Department of Physics and Astronomy, Iowa State University, Ames, Iowa 50011, USA.

⁵Department of Physics, University of Alabama at Birmingham, Birmingham, AL 35294-1170, USA.

(Dated: August 9, 2023)

A recently emerging concept for quantum phase discovery is the controlled gapping of linear band crossings in topological semimetals. For example, achieving topological superconducting and charge-density-wave (CDW) gapping could introduce Majorana zero modes and axion electrodynamics, respectively. Light engineering of correlation gaps in topological materials provides a new avenue of achieving exotic topological phases inaccessible by conventional tuning methods such as doping and straining. Here we demonstrate a light control of correlation gaps and ultrafast phase switchings in a model CDW and polaron insulator $(\text{TaSe}_4)_2\text{I}$ recently predicted to be an axion insulator. Our ultrafast terahertz photocurrent spectroscopy reveals a two-step, non-thermal melting of polarons and electronic CDW gap via studying the fluence dependence of a *longitudinal* circular photogalvanic current. The helicity-dependent photocurrent observed along the propagation of light reveals continuous ultrafast switchings from the polaronic state, to the CDW (axion) phase, and finally to a hidden Weyl phase as the pump fluence increases. Other distinguishing features corroborating with the light-induced switchings include: mode-selective coupling of coherent phonons to polaron and CDW modulation, and the emergence of a *non-thermal* chiral photocurrent above pump threshold of CDW-related phonons. The ultrafast chirality control of correlated topological states revealed here is important to realize axion electrodynamics and quantum computing.

Ultrafast laser excitation has emerged as an important approach to tune and realize dynamical topological phase switching of functionalities, e.g., light-induced Floquet-Weyl semimetal phase[1], and light-induced Dirac/Weyl nodes[2–4]. Thus far, the light-control concept has been mainly realized in a nearly free fermion context due to the weak electron-phonon (*e-p*) and electron-electron (*e-e*) interactions in related topological materials[5]. An exciting recent research development in condensed matter is the possibility to search for new physics emerging from the interplay between strong correlation and Dirac/Weyl points. For example, strong *e-p* or *e-e* coupling in topological materials has the chances to drive a complex phase diagram with symmetry-broken ground states which may embed exotic topological responses[6, 7]. As illustrated in Fig. 1b, a topological Weyl semimetal with quasi-one-dimensional (quasi-1D) lattice could develop multiple correlated states, ranging from a gapped polaron state, an insulating charge-density-wave (CDW) state, to a gapless Weyl semimetal state, depending on the *e-p* coupling strength and temperatures[8–10]. Intriguingly, an insulating CDW state realized in a Weyl semimetal has been argued to be a new avenue to construct a topological axion insulator phase in contrast to previous attempts mainly based on fabricating quantum anomalous Hall sandwich heterostructures[11, 12]. This rich phase

competition is expected to give rise to more novel physics if these correlated topological phases can be tuned accurately and continuously. Ultrafast excitations of complex multi-component order parameters and across the correlation gaps provide a fascinating opportunity to generate and distinguish topological phases and tune their competitions. However, to date, experimental demonstration of ultrafast photo-tuned correlated topological states remains scarce.

$(\text{TaSe}_4)_2\text{I}$ represents a unique setting of correlated topological Weyl semimetals for light-topology quantum control of correlated topological phases. $(\text{TaSe}_4)_2\text{I}$ is a prototypical quasi-1D Peierls system that develops an incommensurate CDW state below $T_{\text{CDW}} \sim 260$ K[13, 14]. The formation of electronic CDW gaps wipes out the Weyl node pairs by mixing their chiralities[10, 15], which introduces a topological axion term $\theta \mathbf{E} \cdot \mathbf{B}$ into the phase dynamics of the complex CDW order parameter[6]. Here θ is the effective axion field. \mathbf{E} and \mathbf{B} are the electric and magnetic fields. As a result, this unusual gapped Weyl state is predicted to be an axion insulator, a novel topological phase with zero Chern number to realize the long-sought quantized topological magnetoelectric effect and axion electrodynamics[16]. Despite the exciting promise, an outstanding challenge to realize such exotic topological phases in $(\text{TaSe}_4)_2\text{I}$ is the poor screening of the strong

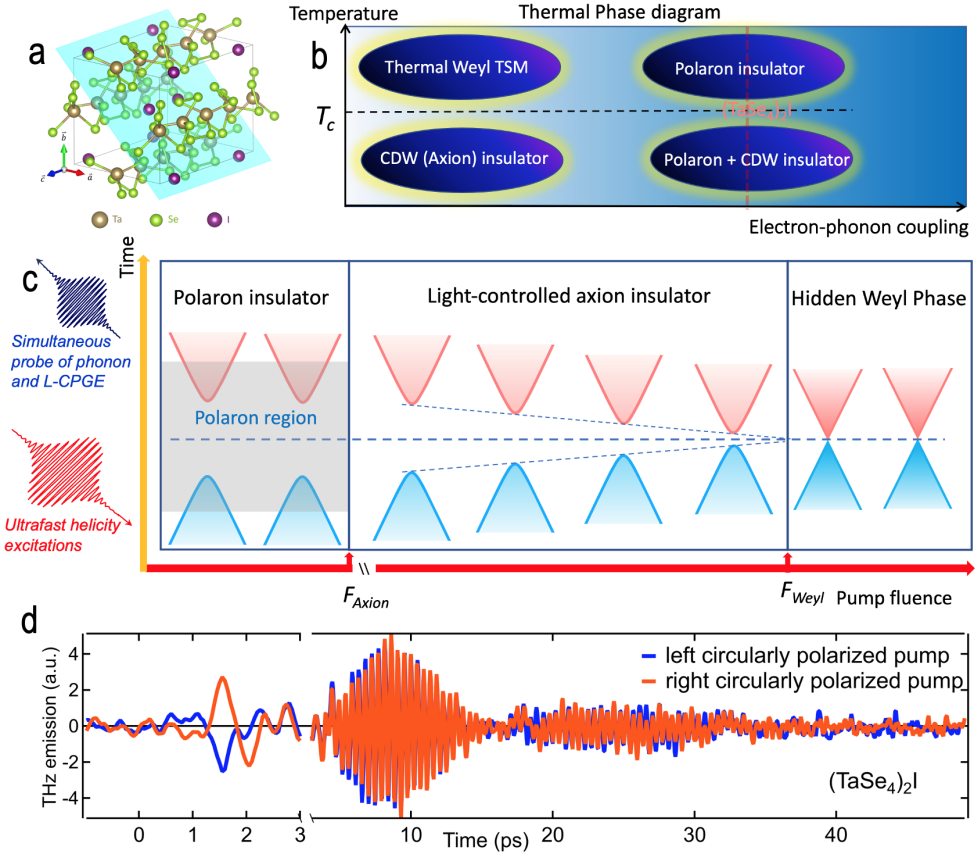


FIG. 1: **Light control of phase switchings in a correlated CDW-Weyl semimetal.** **a**, Lattice structure of $(\text{TaSe}_4)_2\text{I}$. The highlighted light blue surface is the natural cleavage plane. **b**, Phase diagram of topological quasi-1D CDW system as functions of electron-phonon coupling strength and temperature. The strong electron-phonon coupling in $(\text{TaSe}_4)_2\text{I}$ drives a polaron state which preempts the axion (CDW) insulator phase and the thermal Weyl phase. **c**, A schematical illustration of the two-step light melting of polaron state and CDW phase, as well as the light-induced topological phase switching from an axion insulator state to a hidden Weyl phase. **d**, A representative polarized THz emission data along \hat{k} after circularly polarized laser excitations with 800 nm central wavelength and 40 fs pulse duration in the single crystal $(\text{TaSe}_4)_2\text{I}$. The data were taken at 5 K and the pump fluence of 1 mJ/cm^2 .

e - p coupling due to the low lattice dimensionality. Consequently, even in normal state, the charge carriers in $(\text{TaSe}_4)_2\text{I}$ are always dressed with lattice vibrations and turn into polarons which have vanishing spectral weight and extremely short coherence length[8, 9, 15, 17]. As illustrated in Fig. 1b, the high-temperature phase of $(\text{TaSe}_4)_2\text{I}$ is actually a polaron insulator, and the low-temperature phase is a polaron plus CDW insulator, pre-empting both the thermal Weyl phase and the axion insulator phase[8, 9, 15, 17]. Recent intense debates on if $(\text{TaSe}_4)_2\text{I}$ is a true axion insulator based on dc magnetotransport measurements may arise from this ubiquitous polaron physics in $(\text{TaSe}_4)_2\text{I}$ [16, 18].

In this work, we propose and demonstrate an experimental approach to accurately access, tune, and characterize the genuine exotic topological states in $(\text{TaSe}_4)_2\text{I}$ hidden by polaron physics. Owing to the ultralow amplitude mode frequency [19, 20], the ultrafast responses of electronic and lattice components of the CDW phase in

$(\text{TaSe}_4)_2\text{I}$, i.e., the charge order and the periodic lattice distortion, will have to be extremely decoupled[21, 22]. Our experimental approach, polarization-resolved THz emission spectroscopy, is able to simultaneously capture three complementary aspects of the correlated phase tuning: (1) the melting of polaron and CDW gaps is captured by the ultrafast photocurrent emission in the sub-ps time scale; (2) the ultrafast response of the periodic lattice distortion is captured by the phonon emission in the tens of ps time scale; (3) and most importantly, $(\text{TaSe}_4)_2\text{I}$ is a topological Weyl semimetal with a chiral lattice structure (SG97). It is predicted to intrinsically carry the quantized circular photogalvanic effect (CPGE)[15, 23]. The longitudinal component L-CPGE, a parallel or anti-parallel photocurrent along \hat{k} upon different circularly polarized pump, directly correlates with the geometrical chirality that guarantees the existence of topological Weyl fermions (see Methods)[23, 24]. Thus, the recovery dynamics of geometric band chirality gapped

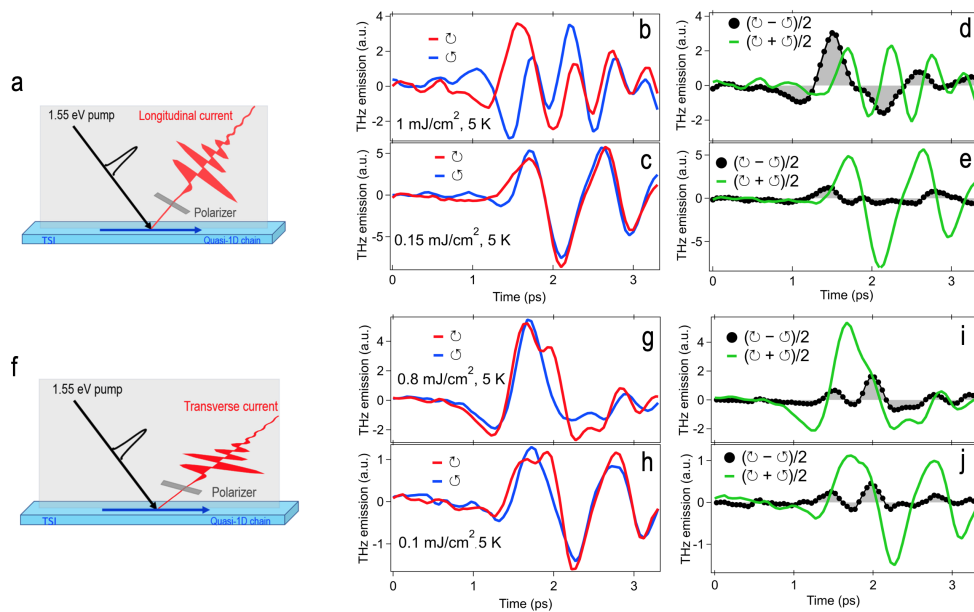


FIG. 2: **A longitudinal circular photogalvanic current probed by polarized THz emission spectroscopy.** The measurement geometry for the longitudinal (a) and transverse (f) CPGE photocurrent. The incidence angle of fs laser excitation is 45 degrees. The incidence plane is set parallel to the c -axis chain and perpendicular to the natural cleavage plane. A few THz polarizers are used to selectively probe the desired THz emission components. THz emission in the longitudinal measurement geometry under circularly polarized pump fluence of 1 mJ/cm^2 (b) and 0.15 mJ/cm^2 (c). The decomposition of THz emission into the longitudinal CPGE component $(E_{\odot} - E_{\ominus})/2$ and the component of $(E_{\odot} + E_{\ominus})/2$ under circularly polarized pump fluence of 1 mJ/cm^2 (d) and 0.15 mJ/cm^2 (e). THz emission in the transverse measurement geometry under circularly polarized pump fluence of 0.8 mJ/cm^2 (g) and 0.1 mJ/cm^2 (h). The decomposition of THz emission into the transverse CPGE component $(E_{\odot} - E_{\ominus})/2$ and the component of $(E_{\odot} + E_{\ominus})/2$ under circularly polarized pump fluence of 0.8 mJ/cm^2 (i) and 0.1 mJ/cm^2 (j). The data were taken at 5 K. \odot and \ominus represent right and left circular polarization of pump pulse respectively.

by the correlation gaps in $(\text{TaSe}_4)_2\text{I}$ can be measured directly by the L-CPGE photocurrent as the polaron and CDW gaps are continuously melted.

The configurations of our THz emission experiment are illustrated in Fig. 2a and 2f. The incidence plane is parallel to the chain direction (c axis) and perpendicular to the natural cleavage plane (Fig. 1a). These configurations are designed to detect both longitudinal (L-) and transverse (T-) CPGE photocurrents along the directions \hat{k} (Fig. 2a) and $\hat{k} \times \hat{c}$ (Fig. 2f), respectively. We show one representative polarized THz emission set of data along \hat{k} in Fig. 1d. This dataset is measured at 5 K and 1 mJ/cm^2 under the longitudinal geometry (Fig. 2a). The THz emission temporal profiles exhibit a nearly single cycle oscillation in the first few ps, and the multi-cycle long-lasting oscillations and beatings in the subsequent extended tens of ps time scale. These behaviors clearly disentangle the *fast electronic* from the *slow phononic* components via their very different generation and relaxation times. Since the photo-excited hot electrons are expected to quickly relax to Fermi level and band edges within 10s of fs, the much longer-lived, ps photocurrent component should originate from the flow of electrons in the bands near the Fermi level, which intrinsically carries the information of the ultrafast melting of electronic

gaps. The even longer-lasting oscillatory component is determined by structural dynamics of the CDW-related zone-folding phonons[19, 25]. Remarkably, as the helicity of the optical pump pulse is reversed, the ps photocurrent emission component experiences a π phase shift that indicates a significant L-CPGE photocurrent, consistent with the prediction of CPGE in $(\text{TaSe}_4)_2\text{I}$ [15, 23]. This behavior represents a benchmark that photoexcitations transfer their net helicities to Weyl fermions flowing in bands with definite chirality[26–28]. In contrast, the phonon emission component is independent of the helicity of the optical pump pulse.

We now present evidence to underpin a light control of ultrafast phase switchings via a non-thermal quench of correlation gaps. In Fig. 2b to 2e, we compare the L-CPGE photocurrent in $(\text{TaSe}_4)_2\text{I}$ for two pump fluence 0.15 and 1 mJ/cm^2 . Here, we emphasize two points. First, we observe a distinct pump fluence dependence that shows the non-thermal effect. Under weak pump fluence (Fig. 2c), the difference of the polarized THz emission profiles between left (\ominus) and right (\odot) circularly polarized pump is small, indicating a weak L-CPGE current. In contrast, under strong pump fluence (Fig. 2b), the difference of THz emission is significantly enhanced. To highlight the L-CPGE photocurrent, we

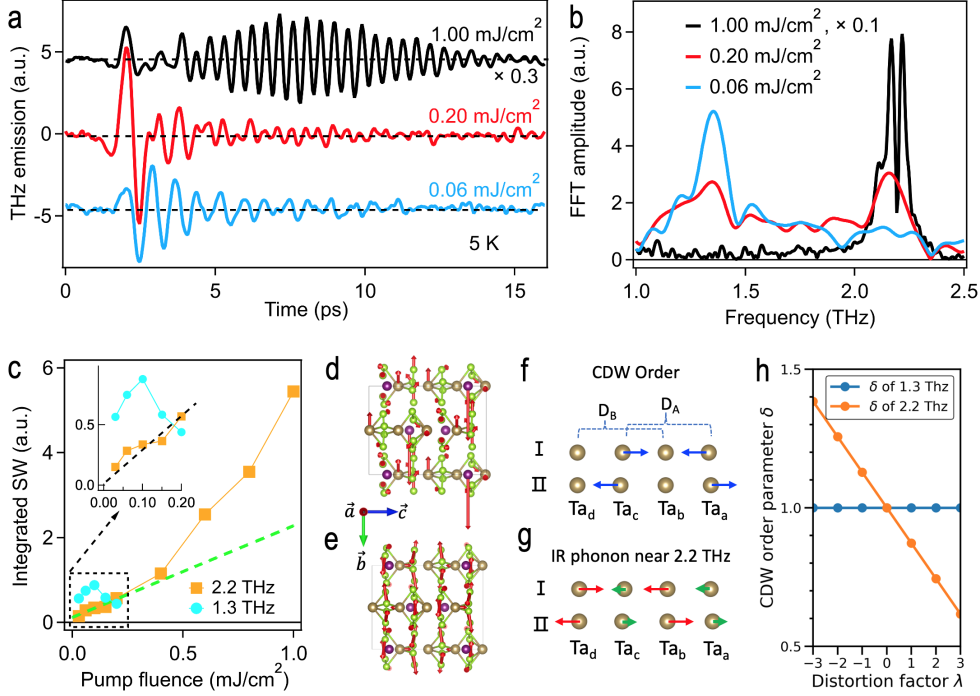


FIG. 4: **Mode-selective phonon emission as evidence for light control of the correlated topological phases in $(\text{TaSe}_4)_2\text{I}$.** (a) THz phonon emission as a function of sampling time delay under pump fluence of 0.06, 0.20 and 1.00 mJ/cm^2 . The linearly polarized excitation laser pulse is set perpendicular to the chain. The THz emission is probed in the geometry shown in Fig. 2(a). (b) The magnitude of fast Fourier transformation of the phonon emission component. (c) The integrated spectral weight of phonon modes as a function of pump fluence. The inset highlights the fluence dependence of phonon spectral weight at low pump fluence. The crystal structure with eigenvectors of B_2 IR phonon near 1.3 THz (d) and B_3 IR phonon near 2.2 THz (e) shown from side (100) view. Atom types of $(\text{TaSe}_4)_2\text{I}$ are with the following colors: golden, Ta; green, Se; purple, I. The arrows indicate the direction and magnitude of the atomic displacements of the corresponding phonon mode. (f) Ta atom pair of CDW phase, the blue arrows show the CDW order: atoms displacement from non-CDW phase to CDW phase. D_A is the distance between Ta_a and Ta_c along c -axis. D_B is the distance between Ta_b and Ta_d along c -axis. (g) Ta atom pair of B_3 IR phonon near 2.2 THz. The red arrows show large displacements of Ta_b and Ta_d . The green arrows show small displacements of Ta_a and Ta_c . (h) Phonon distortion dependence of CDW order parameter δ for B_2 IR phonon near 1.3 THz (blue curve) and B_3 IR phonon near 2.2 THz (orange curve), respectively.

ture used. Fig. 3c and 3d focus on the pump fluence dependence of the photoinduced longitudinal CPGE/LPGE magnitude above $0.4 \text{ mJ}/\text{cm}^2$. The room-temperature CPGE/LPGE value is nearly fluence independent, pointing to a thermal Weyl phase recovered by the one-step light melting of polarons. In contrast, the 5 K magnitude shows a sharp increase above $0.4 \text{ mJ}/\text{cm}^2$ and a plateau beyond $0.8 \text{ mJ}/\text{cm}^2$. This distinguishing feature allows us to clearly single out the salient non-thermal phase switching from a true axion insulator phase (hidden by polarons) to a hidden Weyl state. Note that the CPGE/LPGE magnitude contributed from the hidden Weyl state significantly overtakes (three times of) the magnitude from the thermalized Weyl phase, signifying a unique light-driven Weyl state in the low-temperature phase.

Next, we show the selective excitation of the different phonon modes above (below) F_{Axion} that reveals the difference between the light-induced phases under low and

high pump fluences. Fig. 4a shows coherent phonon emissions at 5 K for three pump fluences. Interestingly, the long-lasting oscillatory profile shows strong pump fluence dependence. At pump fluence far below F_{Axion} , the photocurrent component is extremely weak. The phonon emission dominates the entire THz emission profile. This observation is consistent with the scenario that an insulating polaron state exists close to equilibrium and is robust at low pump fluences. The fast Fourier transform (FFT) spectrum of this coherent signal exhibits a clear resonance at $\sim 1.3 \text{ THz}$ (aqua, Fig. 4b), which matches well with the B_2 IR phonon mode revealed by the linear optical response of equilibrium state[30, 31]. In contrast, at pump fluence far above F_{Axion} , a pronounced multi-cycle beating signal becomes significant (see complete dataset in SI). The FFT spectra of these coherent beatings display multiple dominant peaks centered at $\sim 2.2 \text{ THz}$ (black, Fig. 4b). These modes are zone-folding phonons associated with the periodic lattice distortion

of the CDW transition in $(\text{TaSe}_4)_2\text{I}$ (see more dataset in SI). Our analysis shows they have a B_3 IR symmetry which are found negligibly small in the linear response of ground state[32]. At the polaron melting threshold F_{Axion} , we see a co-existence of both modes in Fig. 4a and 4B, while the B_2 mode is significantly suppressed comparing to low pump fluences. The suppression of B_2 mode at 1.3 THz correlates with the light melting of polaron state, which revives the desired exotic topological phases inaccessible by conventional tuning methods. Fig. 4c summarizes the pump fluence dependence of the coherently excited phonon spectral weight at B_2 and B_3 symmetries. Most intriguingly, the B_3 modes exhibit a clear linear to nonlinear transition (Fig. 4c) near F_{Axion} that strongly correlates with the suppression of B_2 phonon mode. This crossover indicates the light modulation of the CDW order, which is equivalent to the light engineering of the axion insulator phase in a Weyl-CDW system, starts to dominate the ultrafast response as the polaron state is melted. Furthermore, the switching between the polaron- to CDW-related coherent phonons in Fig. 4c strongly correlates with the emergence of a significant *non-thermal* chiral current as CPGE/LPGE amplitude in Fig. 3c. Therefore, the selective excitation of the B_3 (B_2) mode above (below) F_{Axion} validates our conclusion that the light-induced topological phases like the axion insulator state and the hidden Weyl phase are distinguished from the equilibrium and/or thermalized Weyl phase by different collective oscillations associated with it. It is worth noting that above the melting fluence of the electronic charge order, the spectral weight of B_3 modes still increases. This inconsistency of melting fluence corroborates with their decoupling nature after photoexcitation on the time scale of electron-phonon thermalization. In some extreme circumstances such as in the prototype quasi-1D CDW system $\text{K}_{0.3}\text{MoO}_3$, the melting fluence of the periodic lattice distortion is ten times higher than the melting fluence of the electronic density modulation[33].

To put the mode-selective coupling in the CDW and non-CDW phases on firm ground, we carry out IR phonon spectra calculations based on density functional theory (DFT)[34] (see Methods and SI). In Fig. 4d and 4E, we illustrate the eigenmodes of the B_2 IR phonon near 1.3 THz and the B_3 IR phonon near 2.2 THz in the CDW phase. To facilitate the study of phonon coupling to CDW order, we define a CDW order parameter as $\delta = (D_A - D_B)/(D_A^0 - D_B^0)$, where D_A and D_B are Ta atom pair distances as schematically illustrated in Fig. 4f and 4g, and D_A^0 and D_B^0 denote the equilibrium distances[35]. As shown in Fig. 4h, the CDW order parameter δ can be modulated linearly with the B_3 phonon displacement, while it is inert to the B_2 mode. In consistency with the experiments, this selective coupling suggests that the strong B_3 mode oscillation can disturb the CDW phase and assist a dynamical phase transition. We

further estimate the sensitivity of the B_2 IR phonon to different phases by comparing the intensity in the CDW and non-CDW phases. The calculated B_2 (nearly two-fold degenerate) phonon intensity in the CDW phase is found to be close to that of the associated phonon in non-CDW phase (see SI), in consistency with the observation that the B_2 mode is decoupled from the CDW order.

In summary, we have discovered a light-induced phase switching in a correlated topological materials and demonstrated an ultrafast chirality control enabled by fs circularly polarized excitations. The observation of the longitudinal CPGE photocurrent in $(\text{TaSe}_4)_2\text{I}$ reveals the presence of geometrical chirality associated with the multiple light-driven phases, at intermediate and high pump fluence, respectively. Our results open opportunities to discover and control hidden topological quantum phases that are inaccessible via “slow” thermodynamic tuning methods. The characterization and control scheme of chirality and correlation may represent a universal principle to induce quantum geometry and non-trivial topology of electronic bands in strong correlated materials, which connects an entire field of strongly correlated electronic materials with topological phenomena.

METHODS

THz emission spectroscopy. The setup of THz emission spectroscopy is driven by a Ti-sapphire amplifier with 800 nm central wavelength, 1 kHz repetition rate and 40 fs pulse duration. Technical details can be found elsewhere [36–39]. The laser is split into two beams. One is used to photoexcite the $(\text{TaSe}_4)_2\text{I}$ sample at a 45 degree incidence angle. The incidence plane is set parallel to the *c*-axis chain and perpendicular to the natural cleavage plane (see Fig. 1b and 2a). The other beam is used to measure the emitted THz pulse in the time domain by electro-optic sampling through a 1 mm ZnTe crystal. A quarter waveplate is placed in the pump beam in order to change the polarization, that is, helicity, of the pump beam. In front of the THz electro-optic sampling crystal ZnTe, a few THz polarizers are used to measure the desired polarization component of THz photocurrent emission, either parallel or perpendicular to the plane of incidence (highlighted in Fig. 2a and 2f).

THz detection bandwidth. We use a laser system with 800 nm central wavelength, 1 kHz repetition rate and 40 fs pulse duration to generate and detect THz pulse. We had tested the detection bandwidth of our system. We used a ZnTe crystal to generate THz pulse, and then let the THz pulse go through a 1 mm pinhole. Finally the THz pulses is detected by a second ZnTe crystal. We found our THz detection bandwidth is optimized between 0.5 to 2.5 THz. We provide calibration data in supplementary information. Therefore, it is not surprising to see that our THz system does not resolve any 0.1 and 0.2 THz mode since they are outside of our detection bandwidth[19, 20, 40].

Sample growth. The $(\text{TaSe}_4)_2\text{I}$ crystals were grown by chemical vapor transport method. Starting materials of Ta powder (99.9%, Macklin), Se granules (99.999%, Aladdin) and Iodine (99.99%, Aladdin) were mixed in a molar ratio of 1: 4: 1, loaded into an alumina crucible, and then was sealed in a quartz ampoule under partial argon atmosphere. The assembly was heated up in a two-zone furnace with high and low temperature sides being 550°C and 400°C, respectively. The sample was slowly heated up to the

target temperatures in 5 hours, and stayed for 200 hours before naturally cooling down. Finally, the assembly was taken out from the furnace. Strip like crystals could be found in the cold zone with a typical size of $\sim 1 \times 1 \times 5 \text{ mm}^3$.

Correlation of the measured L-CPGE photocurrent to band chirality in $(\text{TaSe}_4)_2\text{I}$. $(\text{TaSe}_4)_2\text{I}$ has a quasi-1D body-centered tetragonal chiral lattice structure in SG97 ($I422$) that lacks improper rotation symmetries, such as inversion or mirror symmetry[15]. Band structure calculation shows there are 24 pairs of Weyl points near the Fermi energy. All these Weyl points are located within a close vicinity of the $k_z = \pm\pi/c$ planes[15]. The CDW phase transition will gap all Weyl points below the Fermi energy. Because the Weyl points with opposite chiral charges appear at different energies, $(\text{TaSe}_4)_2\text{I}$ is predicted to exhibit circular photogalvanic effect (CPGE). Most remarkably, the CPGE in $(\text{TaSe}_4)_2\text{I}$ could be quantized, which is the bulk signature of topological chirality[15, 23]. The longitudinal component L-CPGE, a parallel or anti-parallel photocurrent along \hat{k} upon different circularly polarized pump, directly correlates with geometrical band chirality which guarantees the existence of topological Weyl fermions[23, 24].

The equilibrium phase diagram of $(\text{TaSe}_4)_2\text{I}$. The insulating polaronic state at equilibrium is well-established by several static and time-resolved ARPES measurements[8, 9, 15, 17]. The sample growth process of the $(\text{TaSe}_4)_2\text{I}$ crystal will more or less introduce some defects and self-doping effects which drive the Fermi level a little further away from the CDW gap region. As shown in Fig. S15 of the referred Nature Physics paper[15], above and far below the CDW transition temperature T_{CDW} , one can always observe a robust energy gap near the Fermi energy. This gap is referred to the polaron gap and is induced by strong electron-phonon coupling. The real CDW gap ($\sim 0.2 \text{ eV}$) is actually below the polaron gap. A more exciting and persuasive introduction of polaron physics in $(\text{TaSe}_4)_2\text{I}$ is given by this recent time-resolved ARPES work[17]. Note that the size of the polaron gap is basically the same both at room temperature and far below T_{CDW} . This feature could exclude some other possibilities, such as a fluctuating CDW above T_{CDW} . It is hard to believe that in the deep and well-developed CDW phase (like at 5 K), a fluctuating CDW may still exist to generate a pseudogap just above the well-developed CDW gap. Therefore, our phase diagram of $(\text{TaSe}_4)_2\text{I}$ at equilibrium precisely describes the physics in this model quasi-1D CDW system.

Some other THz generation mechanisms and their relevance to $(\text{TaSe}_4)_2\text{I}$. Besides the longitudinal circular photogalvanic effect, other mechanisms, such as the photo-Dember effect, photon drag effect and photo-thermoelectric effect, could be able to contribute THz photocurrent emission too. With further measurements, we could exclude all these sources and underpin the main contribution of the longitudinal circular photogalvanic effect. THz emission may arise from the photon drag effect not involving material symmetry-breaking[41]. To exclude such an effect, one should measure THz emission with normal incident pump and see whether the THz emission signal is negligible or notable in this geometry. If the THz emission is only from the photon drag effect, one should observe THz emission signal with oblique incident pump and negligible THz emission signal with normal incident pump. We show our THz emission data with oblique incident pump and normal incident pump in supplementary information. Our THz emission data with normal incident pump is comparable to that with 45 deg oblique incident pump, which cannot be explained by the photon drag effect. Moreover, our pump fluence dependent CPGE effect as presented in Fig. 3a of our main text shows a clear linear to non-linear saturation, which cannot be explained by the photon drag effect either. Therefore, the photon drag effect can be safely ruled out in our case. Additionally, the photo-Dember effect and photo-thermoelectric effect can be ruled out too. They both are pump polarization independent and is directed perpendicular to the sample surface, so that the normal incidence geometry cannot measure it[42, 43].

Computational Method and model system. The first-

principles density functional theory (DFT) were performed using projector augmented wave (PAW) pseudopotentials with exchange functions Perdew-Burke-Ernzerhof (PBE) implemented in the VASP package[34]. In this work, we use Γ -centered k-point mesh $3 \times 3 \times 2$ and set plane-wave cutoff energy as 400 eV. The spin-orbit coupling (SOC) effect is included in all calculations. $(\text{TaSe}_4)_2\text{I}$ forms a tetragonal chiral crystal structure with space group $I422$ (No. 97) under ambient conditions, with lattice parameters $a = 9.531 \text{ \AA}$ and $c = 12.824 \text{ \AA}$. In order to obtain crystal structure of non-CDW, we fully relaxed the crystal structure in both the lattice constants and atomic positions until the force on each atom was smaller than 0.01 eV/\AA . By distorting along the lowest negative phonon of non-CDW and then do full relaxation, we obtain the crystal structure of CDW phase with space group $F222$ (No.22). [35]. Phonons and infrared spectroscopy are calculated by the finite displacement method via Phonopy and Phonopy-Spectroscopy package.

Data availability. All relevant data are available on reasonable request from J.W.

-
- [1] Hubener, H., Sentef, M. A., Giovannini, U. D., Kemper, A. F. & Rubio, A. Creating stable floquet-Weyl semimetals by laser-driving of 3D Dirac materials. *Nat. Commun.* **8**, 13940 (2017).
 - [2] Sie, E. J. *et al.* An ultrafast symmetry switch in a Weyl semimetal. *Nature* **565**, 61 (2019).
 - [3] Vaswani, C. *et al.* Light-driven raman coherence as a non-thermal route to ultrafast topology switching in a Dirac semimetal. *Phys. Rev. X* **10**, 021013 (2020).
 - [4] Luo, L. *et al.* A light-induced phononic symmetry switch and giant dissipationless topological photocurrent in ZrTe_5 . *Nat. Mater.* **20**, 329 (2019).
 - [5] Armitage, N. P., Mele, E. J. & Vishwanath, A. Weyl and Dirac semimetals in three-dimensional solids. *Rev. Mod. Phys.* **90**, 015001 (2018).
 - [6] Wang, Z. & Zhang, S.-C. Chiral anomaly, charge density waves, and axion strings from Weyl semimetals. *Phys. Rev. B* **87**, 161107 (2013).
 - [7] Sehayek, D., Thakurathi, M. & Burkov, A. A. Charge density waves in Weyl semimetals. *Phys. Rev. B* **102**, 115159 (2020).
 - [8] Perfetti, L. *et al.* Spectroscopic indications of polaronic carriers in the quasi-one-dimensional conductor $(\text{TaSe}_4)_2\text{I}$. *Phys. Rev. Lett.* **87**, 216404 (2001).
 - [9] Tournier-Colletta, C. *et al.* Electronic instability in a zero-gap semiconductor: The charge-density wave in $(\text{TaSe}_4)_2\text{I}$. *Phys. Rev. Lett.* **110**, 236401 (2013).
 - [10] Zhang, Y., Lin, L.-F., Moreo, A., Dong, S. & Dagotto, E. First-principles study of the low-temperature charge density wave phase in the quasi-one-dimensional Weyl chiral compound $(\text{TaSe}_4)_2\text{I}$. *Phys. Rev. B* **101**, 174106 (2020).
 - [11] Xiao, D. *et al.* Realization of the axion insulator state in quantum anomalous Hall sandwich heterostructures. *Phys. Rev. Lett.* **120**, 056801 (2018).
 - [12] Liu, C. *et al.* Robust axion insulator and Chern insulator phases in a two-dimensional antiferromagnetic topological insulator. *Nat. Mater.* **19**, 522 (2020).
 - [13] Incommensurate superlattice reflections in quasi one dimensional conductors, $(\text{MSe}_4)_2\text{I}$ (M=Ta and Nb). *Solid State Communications* **49**, 313–316 (1984).
 - [14] Gressier, P., Whangbo, M. H., Meerschaut, A. & Rouxel,

- J. Electronic structures of transition-metal tetrachalcogenides $(MSe_4)_nI$ ($M = Nb, Ta$). *Inorganic Chemistry* **23**, 1221–1228 (1984).
- [15] Shi, W. *et al.* A charge-density-wave topological semimetal. *Nat. Phys.* **17**, 381 (2021).
- [16] Gooth, J. *et al.* Axionic charge-density wave in the Weyl semimetal $(TaSe_4)_2I$. *Nature* **757**, 315 (2019).
- [17] Zhang, Y. *et al.* Bipolaronic nature of the pseudogap in $(TaSe_4)_2I$ revealed via weak photoexcitation. *arXiv:2203.05655* (2022).
- [18] Sinchenko, A. A., Ballou, R., Lorenzo, J. E., Grenet, T. & Monceau, P. Does $(TaSe_4)_2I$ really harbor an axionic charge density wave? *Applied Physics Letters* **120**, 063102 (2022).
- [19] Schaefer, H. *et al.* Dynamics of charge density wave order in the quasi one dimensional conductor $(TaSe_4)_2I$ probed by femtosecond optical spectroscopy. *The European Physical Journal Special Topics* **222**, 1005 (2013).
- [20] Nguyen, Q. L. *et al.* Ultrafast x-ray scattering reveals composite amplitude collective mode in the Weyl charge density wave material $(TaSe_4)_2I$. *arXiv:2210.17483* (2022).
- [21] Eichberger, M. *et al.* Snapshots of cooperative atomic motions in the optical suppression of charge density waves. *Nature* **468**, 799 (2010).
- [22] Hellmann, S. *et al.* Ultrafast melting of a charge-density wave in the Mott insulator 1T-TaS₂. *Phys. Rev. Lett.* **105**, 187401 (2010).
- [23] Chang, G. *et al.* Topological quantum properties of chiral crystals. *Nat. Mater.* **17**, 978 (2018).
- [24] Xu, S.-Y. *et al.* Spontaneous gyrotropic electronic order in a transition-metal dichalcogenide. *Nature* **578**, 545 (2020).
- [25] Schäfer, H., Kabanov, V. V., Beyer, M., Biljakovic, K. & Demsar, J. Disentanglement of the electronic and lattice parts of the order parameter in a 1D charge density wave system probed by femtosecond spectroscopy. *Phys. Rev. Lett.* **105**, 066402 (2010).
- [26] de Juan, F., Grushin, A. G., Morimoto, T. & Moore, J. E. Quantized circular photogalvanic effect in Weyl semimetals. *Nat. Commun.* **8**, 15995 (2017).
- [27] Rees, D. *et al.* Helicity-dependent photocurrents in the chiral Weyl semimetal RhSi. *Science Advances* **6**, eaba0509 (2020).
- [28] Orenstein, J. *et al.* Topology and symmetry of quantum materials via nonlinear optical responses. *Annual Review of Condensed Matter Physics* **12**, 247–272 (2021).
- [29] Ni, Z. *et al.* Giant topological longitudinal circular photogalvanic effect in the chiral multifold semimetal CoSi. *Nat. Commun.* **12**, 154 (2021).
- [30] Degiorgi, L. & Grüner, G. Pinned and bound collective-mode state in charge-density-wave condensates. *Phys. Rev. B* **44**, 7820–7827 (1991).
- [31] Schwartz, A. *et al.* Evidence of charge-density-wave fluctuations in the low frequency optical conductivity of $K_{0.3}MoO_3$ and $(TaSe_4)_2I$. *Ferroelectrics* **176**, 309–319 (1996).
- [32] Sherwin, M. S., Zettl, A. & Richards, P. L. Complete excitation spectrum for a charge-density-wave system. *Phys. Rev. B* **36**, 6708–6711 (1987).
- [33] Tomeljak, A. *et al.* Dynamics of photoinduced charge-density-wave to metal phase transition in $K_{0.3}MoO_3$. *Phys. Rev. Lett.* **102**, 066404 (2009).
- [34] Kresse, G. & Furthmüller, J. Efficient iterative schemes for ab initio total-energy calculations using a plane-wave basis set. *Phys. Rev. B* **54**, 11169–11186 (1996).
- [35] Zhang, Y., Lin, L.-F., Moreo, A., Dong, S. & Dagotto, E. First-principles study of the low-temperature charge density wave phase in the quasi-one-dimensional Weyl chiral compound $(TaSe_4)_2I$. *Phys. Rev. B* **101**, 174106 (2020).
- [36] Cheng, D. *et al.* Helicity-dependent terahertz photocurrent and phonon dynamics in hybrid metal halide perovskites. *J. Chem. Phys.* **151**, 244706 (2019).
- [37] Liu, Z. *et al.* Helicity-dependent terahertz photocurrent and phonon dynamics in hybrid metal halide perovskites. *Crystals* **12**, 1462 (2022).
- [38] Luo, L. *et al.* Quantum coherence tomography of light controlled superconductivity. *Nature Physics* **10.1038/s41567-022-01827-1** (2022).
- [39] Yang, X. *et al.* Ultrafast nonthermal terahertz electro-dynamics and possible quantum energy transfer in the Nb₃Sn superconductor. *Phys. Rev. B* **99**, 094504 (2019).
- [40] Kim, S. *et al.* Observation of a massive phason in a charge-density-wave insulator. *Nat. Mater.* **22**, 429 (2023).
- [41] Cheng, L. *et al.* Giant photon momentum locked THz emission in a centrosymmetric Dirac semimetal. *Science Advances* **9**, eadd7856 (2023).
- [42] Huang, Y. *et al.* Terahertz surface and interface emission spectroscopy for advanced materials. *Journal of Physics: Condensed Matter* **31**, 153001 (2019).
- [43] Lu, W. *et al.* Ultrafast photothermoelectric effect in Dirac semimetallic Cd₃As₂ revealed by terahertz emission. *Nat. Commun.* **13**, 1623 (2022).

ACKNOWLEDGEMENTS:

This work was supported by the U.S. Department of Energy, Office of Basic Energy Science, Division of Materials Sciences and Engineering (Ames National Laboratory is operated for the U.S. Department of Energy by Iowa State University under Contract No. DE-AC02-07CH11358) (topological analysis and DFT calculation). B.C. was supported by the Laboratory Directed Research and Development project, Ames National Laboratory (coherent phonon and photocurrent spectroscopy). Modelling work at the University of Alabama, Birmingham (I.E.P.), was supported by the US DOE under contract no. DE-SC0019137 (Additional interpretation of experimental data). W.X. and Y.-F.G. acknowledge the open project of Beijing National Laboratory for Condensed Matter Physics (Grant No. ZBJ2106110017) and the Double First-Class Initiative Fund of ShanghaiTech University (sample synthesis and basic characterization).

AUTHOR CONTRIBUTIONS:

B.C. and J.W. conceived the project. B.C., D.C., and L.L. performed the THz emission measurements; T.J. and Y.-X.Y. performed first-principles DFT calculations and topological analysis. W.X. and Y. G. developed samples and performed transport characterizations. B.C. and J.W. analyzed the spectroscopy data with the input of L.L., B.-Q.S., M.M., and I.-E.P.; The paper is written by J.W., B.C., T.J., and Y.-X.Y. with discussions from all authors. J.W. supervised the project.

ADDITIONAL INFORMATION:

Supplementary Information accompanies this paper at

Competing financial interests: The authors declare no com-

peting financial interests.

Reprints and permission information is available online at